Depth sectioning with the aberration-corrected scanning transmission electron microscope

Albina Y. Borisevich*, Andrew R. Lupini, and Stephen J. Pennycook

Condensed Matter Sciences Division, Oak Ridge National Laboratory, Oak Ridge, TN 37831

Edited by Frans Spaepen, Harvard University, Cambridge, MA, and accepted by the Editorial Board December 23, 2005 (received for review August 16, 2005)

The ability to correct the aberrations of the probe-forming lens in the scanning transmission electron microscope provides not only a significant improvement in transverse resolution but in addition brings depth resolution at the nanometer scale. Aberration correction therefore opens up the possibility of 3D imaging by optical sectioning. Here we develop a definition for the depth resolution for scanning transmission electron microscope depth sectioning and present initial results from this method. Objects such as catalytic metal clusters and single atoms on various support materials are imaged in three dimensions with a resolution of several nanometers. Effective focal depth is determined by statistical analysis and the contributing factors are discussed. Finally, current challenges and future capabilities available through new instruments are discussed.

aberration correction | electron microscopy | single-atom imaging

The successful implementation of spherical aberration correction in the transmission electron microscope and scanning transmission electron microscope (STEM) is undoubtedly one of the most exciting achievements in electron optics of the last few decades. Correction of magnetic lens aberrations to the third order (1, 2) has led to revolutionary improvements in point resolution and signal-to-noise ratio, expanding the range of accessible lattice spacings into the sub-Ångstrom regime (3) and enabling simultaneous detection of light and heavy elements (4). Before aberration correction, detection of a single atom was a significant achievement (e.g., refs. 5–8), but now these observations are possible and are even becoming routine for a much wider range of materials (9–11). For a microscope equipped with a high-sensitivity aberration-corrected electron energy loss spectrometer, analytical detection of single atoms within a bulk solid has been reported (12).

However, in addition to improvements to existing techniques, aberration correction can enable completely new experiments to be performed, especially when combined with other new developments, such as environmental or *in situ* stages. In particular, the wider probe-forming aperture available after aberration correction gives a reduced depth of focus. The STEM, largely developed by Crewe and coworkers (13) provides the Z-contrast image mode, which, to a good approximation, gives an incoherent image of the sample (14), making it possible to optically section through a sample in a way similar to confocal optical microscopy (15). However, a significant difference from confocal microscopy is that the STEM technique does not use a collection pin-hole, which degrades the depth sensitivity but is more convenient experimentally. The purpose of this paper is to examine the resolution and contrast for the currently available microscopes and demonstrate how 3D data sets can be collected and analyzed for several test systems.

Results and Discussion

Aberration Correction and Depth of Field. The aberration function χ is defined as the deviation of the aberrated wavefront from an ideal (unaberrated) wavefront such that the phase change across the back focal plane of the objective lens is given by $2\pi\chi/\lambda$, for wavelength λ. In STEM field aberrations are normally ignored, so this can be written as (omitting nonrotationally symmetric terms) (2)

$$\chi(\theta) = \frac{1}{2}\,\delta\theta^2 + \frac{1}{4}\,C_s\theta^4 + \frac{1}{6}\,C_5\theta^6 + \frac{1}{8}\,C_7\theta^8 + \cdots, \qquad [1]$$

where θ is the angle to the optical axis, δ is defocus, and C_s, C_5, and C_7 are rotationally symmetric aberrations of the third, fifth, and seventh order, respectively. In an uncorrected microscope, which uses round magnetic lenses, C_s is always positive (16) and approximately constant under standard conditions, whereas defocus can be varied. Aberration correctors use nonround lenses to enable variation of the aberration coefficients to minimize the aberration function and offset the effect of still higher-order terms. The second-generation aberration correctors installed at Oak Ridge National Laboratory (ORNL) can adjust aberrations up to the third order, whereas future correctors will correct aberrations up to the fifth order or higher (17). The lowest-order uncorrectable aberrations will ultimately determine the optimal aperture size θ which in turn determines the best achievable point resolution. For the case of incoherent imaging, the Rayleigh criterion for the diffraction limited case has the form $\Delta r_\perp \approx 0.61\lambda/\theta$, so the resolution scales inversely with the aperture size. Furthermore, increasing the angle θ also affects the depth of field.

The depth of field Δz can be defined numerically in a variety of ways but in incoherent light optics is generally considered to be a range of defocus within which the image contrast does not reduce significantly. Different definitions arise from the different quantitative assessments of what constitutes a significant change of contrast. For example, Born and Wolf (18) suggest the distance within which the intensity on the optic axis stays within 20% of the maximum is a reasonable measure of the focal tolerance. By using the result that for systems with negligible aberrations the intensity on the optic axis obeys the equation

$$I(z) = \left(\frac{\sin\left(\pi \frac{\theta^2}{2\lambda} z \right)}{\pi \frac{\theta^2}{2\lambda} z} \right)^2 I_0, \qquad [2]$$

Born and Wolf (18) show that for this criterion the depth of field Δz can be expressed as

$$\Delta z \approx \frac{\lambda}{\theta^2}. \qquad [3]$$

Conflict of interest statement: No conflicts declared.

This paper was submitted directly (Track II) to the PNAS office. F.S. is a guest editor invited by the Editorial Board.

Freely available online through the PNAS open access option.

Abbreviations: BF, bright-field; HAADF, high-angle annular dark-field; ORNL, Oak Ridge National Laboratory; STEM, scanning transmission electron microscopy.

*To whom correspondence should be addressed. E-mail: albinab@ornl.gov.

 www.pnas.org/cgi/doi/10.1073/pnas.0507105103

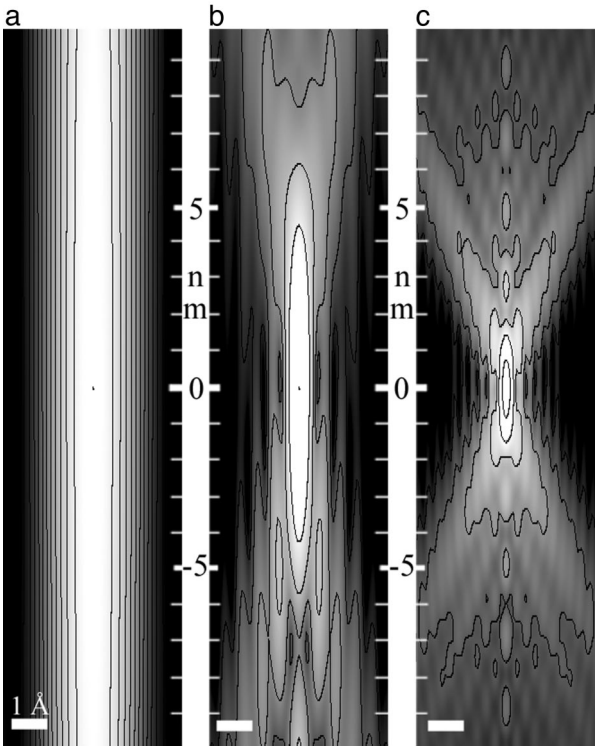

Fig. 1. Probe intensity profiles as a function of defocus for microscopes of three generations; intensities are shown in logarithmic scale with 12 equally spaced logarithmic contours. (*a*) Uncorrected VG501. (*b*) VG603 with a third-order corrector. (*c*) A hypothetical instrument with a C_3/C_5 corrector (see detailed probe parameters in text). Note different scales vertically and laterally. Profiles are shifted vertically so that intensity maxima are at zero defocus.

Thus, with increasing orders of aberration correction and the associated increase in aperture size, the depth of field will decrease very quickly. This change is visualized in Fig. 1, which shows reconstructions of the probe shape in transverse and vertical directions for three microscopes, starting with those at ORNL: the VG HB501UX microscope before correction (Fig. 1*a*) and then the C_3-corrected VG HB603U microscope (Fig. 1*b*) and, finally, a hypothetical future microscope with C_5-corrector (Fig. 1*c*). For the uncorrected 100-kV instrument (Fig. 1*a*) with cold field emission gun (C_3 = 1.3 mm, C_c = 1.3 mm, ΔE = 0.3 eV, θ = 10 mrad), the depth of field as defined by Eq. **3** is ≈45 nm; indeed, over the range of −10 to 10 nm from the maximum intensity, the probe changes very little. For the C_3-corrected, 300-kV microscope (C_3 = −40 μm, C_5 = 10 cm, C_c = 1.6 mm, ΔE = 0.3 eV, θ = 23 mrad), the predicted depth of field is 3.7 nm, suggesting nanometer-scale depth sensitivity. For the hypothetical C_3/C_5-corrected STEM with a monochromator (C_3 = 2.3 μm, C_5 = −2.1 mm, C_7 = 50 cm, C_c = 1.6 mm, ΔE = 0.1 eV, θ = 50 mrad), Eq. **3** gives a 1.0-nm focal tolerance. Changes are also evident laterally: With aberration correction (Fig. 1 *b* and *c*), the probe rapidly becomes sub-Ångstrom. In addition, because the correction is achieved via compensation of the aberration terms of different order, the probe acquires some asymmetry in the vertical direction, most evidently in Fig. 1*b*. On the optic axis intensity decays monotonically in the overfocus region, whereas, in the underfocus region, it decays sharply and forms subsidiary maxima.

Another consequence of the aberration compensation is that the focal depth estimates from the more realistic probe profiles (Fig. 1) are somewhat larger than the estimates from Eq. **3**, which was derived for the symmetric, aberration-free case. For the vertical profile of Fig. 1*b*, the full width at 80% maximum (equivalent to Eq. **3**) is ≈3.9 nm (vs. 3.7 nm), and, for the profile of the Fig. 1*c*, it is ≈1.05 nm (vs. 1.0 nm). These probe profiles incorporate chromatic aberration C_c and gun energy spread ΔE, which also contribute to the probe widening in the vertical direction compared with the aberration-free case.

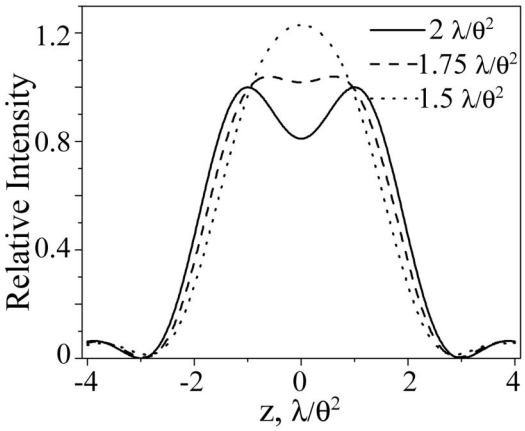

Fig. 2. Vertical profiles of the intensity on the optic axis for the sum of two aberration-free probes with different vertical separations. Defocus *z* is scaled by λ/θ^2.

In the above discussion, the focal depth parameter was used in the traditional sense, i.e., as a vertical range around a perfect defocus value. However, nanometer-scale focal tolerance should enable us to get depth-sensitive information about our samples, enabling a 3D STEM imaging technique akin to confocal optical microscopy. In this case there is no single optimal defocus value, and parameters such as vertical resolution, will be more appropriate for the discussion of the technique's prospects. Resolution can be difficult to define precisely, so we will use an analog of the Rayleigh criterion. In 1879, Rayleigh proposed that "two components of equal intensity should be considered to be just resolved when the principal intensity maximum of one coincides with the first intensity minimum of the other" (18). We can therefore construct a vertical equivalent of Rayleigh's criterion (in an aberration-free approximation) using Eq. **2** to calculate the vertical distance Δz_R between the maximum and the first zero of the intensity on the optic axis as

$$\Delta z_R = 2\,\frac{\lambda}{\theta^2}. \qquad [4]$$

This criterion is illustrated in Fig. 2, which shows vertical profiles of the sum of the two probes focused at various distances from each other (parameterized by λ/θ^2). Thus, even currently available microscopes are potentially capable of resolving objects directly above one another just 7–8 nm apart, and, for future generations of microscopes, this capability will improve. The following part of the paper will discuss how these approximate values translate into quantitative 3D information from samples such as catalytic nanoparticles.

First Experiments in 3D Imaging. The discussion above was based on the estimates of the depth sensitivity parameters of the electron probe. These estimates, however, do not translate directly into focal depth and vertical resolution achievable for an arbitrary sample, because many sample-related effects can alter the observed focal depth. At the same time, samples composed of heavy atoms or particles randomly distributed in amorphous or off-axis light matrices should provide the best vehicle for the demonstration of depth-sensing abilities of STEM, because

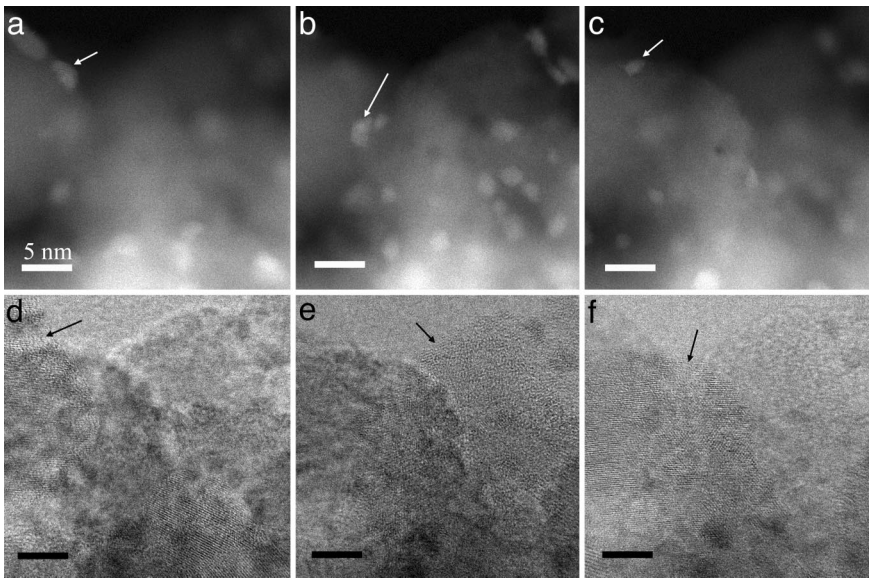

Fig. 3. Frames from the depth series (raw data) acquired by using a VG HB603U from ORNL on a (Pt, Au)/TiO_2 catalyst sample. (*a–c*) HAADF images (detector inner angle, 50 mrad) taken at a distance of −20 nm (*a*), −88 nm (*b*), and −140 nm (*c*) from initial defocus. (*d–f*) The corresponding simultaneously acquired BF images (detector outer angle, 1 mrad). See Movie 1 for the full sequence.

propagation of the beam through the sample results mainly in a simple broadening of the probe. It is therefore possible to treat the 3D data array as a simple convolution of the 3D object function and the 3D probe shape; in this regime, the vertical resolution can achieve its theoretical limit. For the VG HB603U microscope at ORNL, this limit is ≈8 nm (Fig. 1*b*), which is comparable with the scale of many structural features in nanomaterials. Several examples of depth-resolved studies of such samples are given below.

Several frames of a 50-frame focal series collected from TiO_2 powder impregnated with metal nanoparticles (1–3 nm in size and containing Pt and Au at a 1:2 proportion) (19, 20) are given in Fig. 3. High-angle annular dark-field (HAADF) images taken at defocus values of −20, −88, and −140 nm (Fig. 3 *a–c*) show completely different arrangements of metal particles on the substrate. In the −20-nm frame (Fig. 3*a*), a particle in the upper left part of the image (Fig. 3*a*, arrow) appears to be in focus; in the −88-nm frame (Fig. 3*b*), it is very diffuse, and particles in other parts of the image come into focus (Fig. 3*b*, arrow). In the −140-nm frame, most of those particles appear diffuse, and yet another particle (Fig. 3*c*, arrow) comes into focus. Notably, the particles denoted by arrows in Fig. 3 *a* and *c* occupy approximately the same lateral position, but they can be clearly resolved in the vertical direction. Fig. 3 *d–f* show the simultaneously collected bright-field (BF) images. Although the general outline of the TiO_2 flakes stays the same throughout the focal series, the flakes closest to focus are identifiable by the appearance of the phase contrast lattice fringes. Each of the three frames has a different TiO_2 particle in focus (shown by the black arrows); the comparison of the HAADF and BF series suggests that in-focus metal particles are attached to the in-focus TiO_2 flakes. We can therefore attempt a reconstruction of the 3D structure of this powder by using the HAADF intensity to identify metal particle positions and the magnitude of the BF contrast to identify the positions of substrate flakes. The resulting 3D representation (derived from all 50 frames in the focal series; see Movie 1, which is published as supporting information on the PNAS web site) is given in Fig. 4. White, transparent surfaces enclose the areas of increased BF contrast and thus represent TiO_2 flakes; yellow surfaces enclose the areas of the increased HAADF intensity and thus correspond to the metal particles. All of the features indicated on Fig. 3 *a–c* and Fig. 3 *d–f* are also indicated on Fig. 4 by white and black arrows, respectively. The metal particles appear elongated in the depth direction, reflecting the defocus spread of the probe (see Fig. 1*b*). Clearly, deconvolution techniques similar to those used in confocal optical microscopy can help achieve closer correspondence with the real structure of the material. Such a technique will need to take into account the exact values of the residual aberrations and possibly beam broadening on passing through the sample.

Problems similar to the example described in Figs. 3 and 4 are often solved by tilt series STEM tomography, which presently offers superior depth resolution with slightly worse transverse resolution. However, one relevant comparison is that this 50-frame series was recorded in <5 min, although typical tilt series presently take several hours to acquire. More importantly,

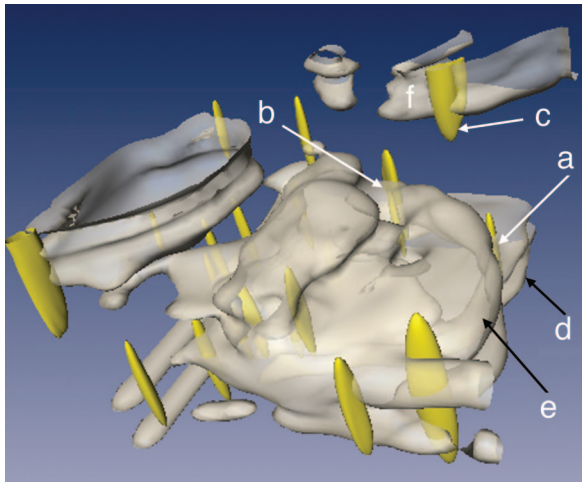

Fig. 4. 3D rendering of the depth series of a (Pt, Au)/TiO_2 catalyst sample. Yellow surfaces enclose the areas of high HAADF intensity and thus represent metal (Pt, Au) particles. White surfaces enclose the areas of high diffraction contrast (from BF series) and thus represent TiO_2 substrate particles. Arrowed features a, b, c, d, e, and f correspond to the arrowed features in Fig. 3 *a*, *b*, *c*, *d*, *e*, and *f*, respectively.

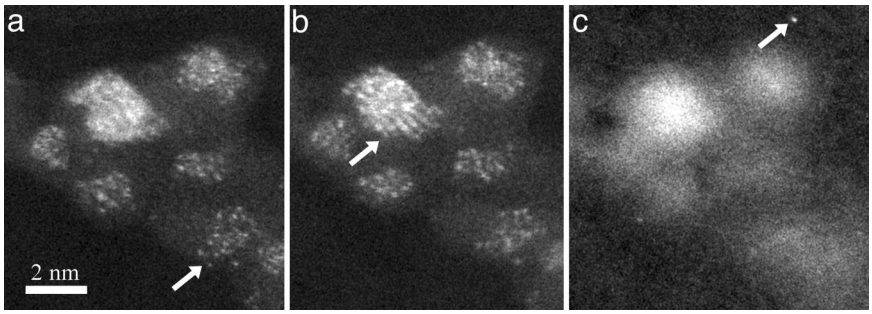

Fig. 5. Frames from the HAADF (detector inner angle, 50 mrad) depth series (smoothed raw data) acquired by using a VG HB603U microscope at ORNL on a (Pt, Ru)/γ-Al_2O_3 catalyst sample at -12 nm (*a*), -16 nm (*b*), and -40 nm (*c*) from initial defocus. See Movie 2 for the full sequence.

tilt-series tomography depends on the validity of the projection approximation (by definition, the depth of field should be greater than the sample thickness) and is therefore constrained to smaller convergence angles, necessarily reducing the point resolution, or requiring extremely thin samples (21). These constraints will become even more limiting for future probes with higher convergence angles, such as the probe on Fig. 1*c*. Not having these limitations, depth slicing can be used for 3D localization of objects as small as one atom and in objects thicker than the depth of focus, producing models of the imaged samples with depth resolution on the order of several nanometers and atomic resolution laterally, as illustrated in the next example.

Fig. 5 shows several frames from a focal series of a sample of γ-Al_2O_3 powder impregnated with $Pt_2Ru_4(CO)_{18}$ (22), dried, and mounted on carbon film. The γ-Al_2O_3 flake is off-axis and appears as a pale blur. In the frame taken at a defocus value of -12 nm (Fig. 5*a*), a thin metal particle (arrow) in the lower right corner appears to be in focus, whereas, in the next frame (defocus -16 nm) (Fig. 5*b*), it is already out of focus and a thicker particle in the upper left corner (Fig. 5*b*, arrow) comes into focus instead. Several steps later, at a defocus of -40 nm (Fig. 5*c*), the γ-Al_2O_3 flakes fade far out of focus, but a single Pt atom (Fig. 5*c*, arrow) is visible attached to the surface of the underlying carbon film.

Single atoms are visible over several adjacent frames (not shown on Fig. 5; see Movie 2, which is published as supporting information on the PNAS web site), which can thus be used to quantitatively analyze the dependence of the incremental intensity on defocus. For the Pt atom on carbon, the incremental intensity was computed from a 2D Gaussian fit of the 25×25 pixel patches of the image containing the atom. The carbon film background was assumed to be flat, and the Pt atom image was assumed to be rotationally symmetric. The resulting dependence is given in Fig. 6. The intensity peaks at approximately -40 nm, but the Pt atom is still quite visible 4 nm away from that defocus; the peak width calculated from Gaussian fit is larger than projected for the probe (full width at 80% maximum of 5.9 nm compared with 3.9 nm; see Fig. 1*b*). This discrepancy could be due to beam broadening upon passing through the carbon film or just the sparse sampling in the depth direction (4-nm steps). Vertical movement of the sample is also a potential problem. Although it is routinely checked (and found negligible) by reproducing one or more of the initial frames after a series is complete, it cannot be monitored in real time.

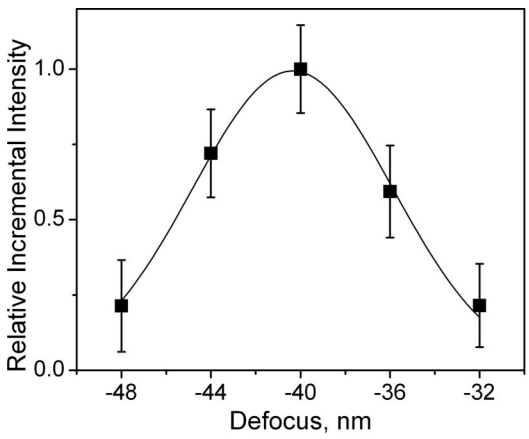

Fig. 6. Variation of the incremental intensity of the single atom from the depth series in Fig. 5 (■). The line is a Gaussian fit.

Error bars on Fig. 6 are equal to the standard deviation of the intensity of the carbon film background away from the metal atoms. At its peak, the Pt atom in Fig. 5*c* is $\approx 7\sigma$ above the background, which results in a wide range of visibility over the noise and thus allows us to make a good estimate of the focal depth. Clearly, the signal-to-noise parameters of images, as well as the quantitative settings of acquisition, will play a major role in the range of visibility of point defects and should be taken into account in data analysis. Any experimental determination of the focal depth should be conducted in such a way as to minimize this influence to obtain a reliable result. The effect of the signal-to-noise ratio on the apparent focal depth was also suggested from observation of single Hf atoms within an amorphous SiO_2 layer (23).

It should however be noted that for an isolated object, such as a single heavy atom on a light support, the precision with which the vertical position could be determined is much better than the vertical resolution of the instrument. If there exists independent evidence that the source is a single atom (e.g., by comparison with other single atom intensities and agreement with total concentration) and sufficient quantitative data can be collected to describe the depth dependence of the associated incremental intensity, the vertical position (i.e., peak center) can be determined by fitting with sub-nanometer accuracy. For example, the Pt atom on carbon film in the series from Fig. 5 can be located at the height of $\approx 40.3 \pm 0.2$ nm with 95% confidence.

It should again be emphasized that with currently available instruments these values of resolution and precision are only achievable for heavy atoms/particles on considerably lighter amorphous or nearly amorphous substrates. Superior depth resolution for similar systems will undoubtedly be achieved for new C_3/C_5 corrected instruments with the predicted focal depth of ≈ 1 nm (Fig. 1*c*). Depth sectioning within aligned crystals is currently out of reach because of electron channeling phenomena (24), meaning the signal from an atom in such a structure depends on the location in a more complicated manner. However, additional simulations show that some depth sectioning in such crystals may become possible in these future instruments, as predicted by Peng *et al.* (25). The simulation details and

PHYSICS

implications are discussed in ref. 26. Deconvolution is also a logical next step.

Conclusions

Aberration correction improves the resolution of scanning transmission electron microscopes by enabling higher convergence angles for the STEM probes. Probe simulations show that the increased convergence angles result in a depth sensitivity of currently available aberration-corrected STEM instruments on the nanometer scale; this sensitivity is expected to improve when the next generation of instrumentation is available.

Initial experiments using a 300-kV VG HB603U with a 23-mrad probe angle demonstrate nanometer-scale depth sensitivity on nanocatalyst samples. Nanometer-sized particles and even single atoms can be localized in three dimensions. Statistical analysis of the data are used to quantify the effective focal depth, which is determined by the probe but also affected by sample parameters, such as signal-to-noise ratios, and image acquisition settings. New microscopes with C_3/C_5 correctors are expected to significantly improve the depth resolution in amorphous and nanoparticulate materials and enable depth sectioning in aligned crystals.

Materials and Methods

Samples were prepared by dispersing catalytic powders onto holey carbon grids. Before imaging, samples were annealed in vacuum at 100°C for 15 min to reduce carbon contamination. STEM observations were made with VG HB603U microscope operated at 300 kV and equipped with Nion (Kirkland, WA) aberration corrector. The microscope parameters were as follows: probe angle, 23 mrad; HAADF detector inner angle, 50 mrad; BF detector outer angle, 1 mrad.

We thank M. Amiridis, R. Adams, O. Alexeev, and L. Ortiz-Soto (all from the University of South Carolina, Columbia) for the provision of catalyst samples. This work was supported by Laboratory Directed Research and Development Program Contract DE-AC05-00OR22725 from the U.S. Department of Energy (managed by UT-Battelle) and by appointments to the Oak Ridge National Laboratory Postdoctoral Research Program administered jointly by the Oak Ridge National Laboratory and the Oak Ridge Institute for Science and Education.

1. Urban, K., Kabius, B., Haider, M. & Rose, H. (1999) *J. Electron Microsc.* **48,** 821–826.
2. Krivanek, O. L., Dellby, N. & Lupini, A. R. (1999) *Ultramicroscopy* **78,** 1–11.
3. Nellist, P. D., Chisholm, M. F., Dellby, N., Krivanek, O. L., Murfitt, M. F., Szilagyi, Z. S., Lupini, A. R., Borisevich, A., Sides, W. H. & Pennycook, S. J. (2004) *Science* **305,** 1741.
4. Chisholm, M. F., Lupini, A. R., Pennycook, S. J., Ohkubo, I., Christen, H. M., Findlay, S. D., Oxley, M. P. & Allen, L. J. (2004) *Microsc. Microanal.* **10,** Suppl. 2, 256–257.
5. Crewe, A. V., Wall, J. & Langmore, J. (1970) *Science* **168,** 1338–1340.
6. Nellist, P. D. & Pennycook, S. J. (1996) *Science* **274,** 413–415.
7. Suenaga, K., Tence, T., Mory, C., Colliex, C., Kato, H., Okazaki, T., Shinohara, H., Hirahara, K., Bandow, S. & Iijima, S. (2000) *Science* **290,** 2280–2282.
8. Voyles, P. M., Muller, D. A., Grazul, J. L., Citrin, P. H. & Gossmann, H. J. L. (2002) *Nature* **416,** 826–829.
9. Pennycook, S. J., Lupini, A. R., Kadavanich, A., McBride, J. R., Rosenthal, S. J., Puetter, R. C., Yahil, A., Krivanek, O. L., Dellby, N., Nellist, P. D. L., *et al*. (2003) *Z. Metallkd.* **94,** 350–357.
10. Varela, M., Lupini, A. R., vanBenthem, K., Borisevich, A. Y., Chisholm, M. F., Shibata, N., Abe, E. & Pennycook, S. J. (2005) *Annu. Rev. Mater. Res.* **35,** 539–569.
11. Wang, S. W., Borisevich, A. Y., Rashkeev, S. N., Glazoff, M. V., Sohlberg, K., Pennycook, S. J. & Pantelides, S. T. (2004) *Nat. Mater.* **3,** 143–146.
12. Varela, M., Findlay, S. D., Lupini, A. R., Christen, H. M., Borisevich, A. Y., Dellby, N., Krivanek, O. L., Nellist, P. D., Oxley, M. P., Allen, L. J. & Pennycook, S. J. (2004) *Phys. Rev. Lett.* **92,** 095502.
13. Crewe, A. V., Wall, J. & Welter, L. M. (1968) *J. Appl. Phys.* **39,** 5861–5868.
14. Pennycook, S. J. & Jesson, D. E. (1991) *Ultramicroscopy* **37,** 14–38.
15. Wilson, T. (1990) *Confocal Microscopy* (Academic, San Diego).
16. Scherzer, O. (1936) *Z. Phys.* **101,** 593–603.
17. Krivanek, O. L., Nellist, P. D., Dellby, N., Murfitt, M. F. & Szilagyi, Z. (2003) *Ultramicroscopy* **96,** 229–237.
18. Born, M. & Wolf, E. (1989) *Principles of Optics: Electromagnetic Theory of Propagation, Interference, and Diffraction of Light* (Pergamon, New York).
19. Mihut, C., Chandler, B. D. & Amiridis, M. D. (2002) *Catal. Comm.* **3,** 91–97.
20. Mihut, C., Descorme, C., Duprez, D. & Amiridis, M. D. (2002) *J. Catal.* **212,** 125–135.
21. Midgley, P. A. & Weyland, M. (2003) *Ultramicroscopy* **96,** 413–431.
22. Alexeev, O. S., Graham, G. W., Shelef, M., Adams, R. D. & Gates, B. C. (2002) *J. Phys. Chem. B* **106,** 4697–4704.
23. vanBenthem, K., Lupini, A. R., Kim, M., Baik, H. S., Doh, S., Lee, J.-H., Oxley, M. P., Findlay, S. D., Allen, L. J., Luck, J. T. & Pennycook, S. J. (2005) *Appl. Phys. Lett.* **87,** 034104.
24. Fertig, J. & Rose, H. (1981) *Optik* **59,** 407–429.
25. Peng, Y. P., Nellist, P. D. & Pennycook, S. J. (2004) *J. Electron Microsc.* **53,** 257–266.
26. Borisevich, A. Y., Lupini, A. R., Travaglini, S. M. & Pennycook, S. J. (2006) *J. Electron Microsc*., in press.

Corrections and Retraction

CORRECTIONS

PHYSICS. For the article "Depth sectioning with the aberration-corrected scanning transmission electron microscope," by Albina Y. Borisevich, Andrew R. Lupini, and Stephen J. Pennycook, which appeared in issue 9, February 28, 2006, of *Proc Natl Acad Sci USA* (103:3044–3048; first published February 21, 2006; 10.1073/pnas.0507105103), the authors note that, due to a printer's error, Fig. 3 appeared incorrectly. When the locants were replaced to meet journal style, surrounding portions of the image were inadvertently distorted. The corrected figure and its legend appear below.

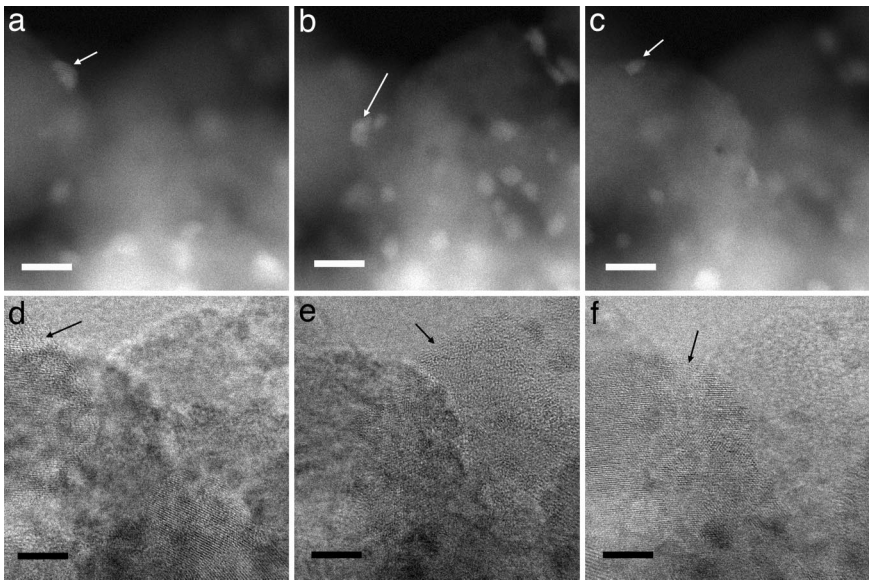

Fig. 3. Frames from the depth series (raw data) acquired by using a VG HB603U from ORNL on a (Pt, Au)/TiO_2 catalyst sample. (*a–c*) HAADF images (detector inner angle, 50 mrad) taken at a distance of −20 nm (*a*), −88 nm (*b*), and −140 nm (*c*) from initial defocus. (*d–f*) The corresponding simultaneously acquired BF images (detector outer angle, 1 mrad). See Movie 1 for the full sequence. (Scale bar, 5 nm.)

www.pnas.org/cgi/doi/10.1073/pnas.0609974103

MEDICAL SCIENCES. For the article "A functional SNP in the promoter of the *SERPINH1* gene increases risk of preterm premature rupture of membranes in African Americans," by Hongyan Wang, Samuel Parry, George Macones, Mary D. Sammel, Helena Kuivaniemi, Gerard Tromp, George Argyropoulos, Indrani Halder, Mark D. Shriver, Roberto Romero, and Jerome F. Strauss III, which appeared in issue 36, September 5, 2006, of *Proc Natl Acad Sci USA* (103:13463–13467; first published August 28, 2006; 10.1073/pnas.0603676103), the authors note that in the Abstract (line 9) and in the first paragraph of *Results* (line 6), the –656 T allele carriage rate in African Americans (12.4%) was reported instead of the intended –656 T allele frequency (7.4%). These errors do not affect the conclusions of the article.

www.pnas.org/cgi/doi/10.1073/pnas.0609705103

MEDICAL SCIENCES. For the article "Germ-line mutations in p27^{Kip1} cause a multiple endocrine neoplasia syndrome in rats and humans," by Natalia S. Pellegata, Leticia Quintanilla-Martinez, Heide Siggelkow, Elenore Samson, Karin Bink, Heinz Höfler, Falko Fend, Jochen Graw, and Michael J. Atkinson, which appeared in issue 42, October 17, 2006, of *Proc Natl Acad Sci USA* (103:15558–15563; first published October 9, 2006; 10.1073/pnas.0603877103), the authors note that in Fig. 3*B*, patient II-1 was incorrectly identified as having parathyroid cancer (PC). The corrected figure and legend appear below. These errors do not affect the conclusions of the article.

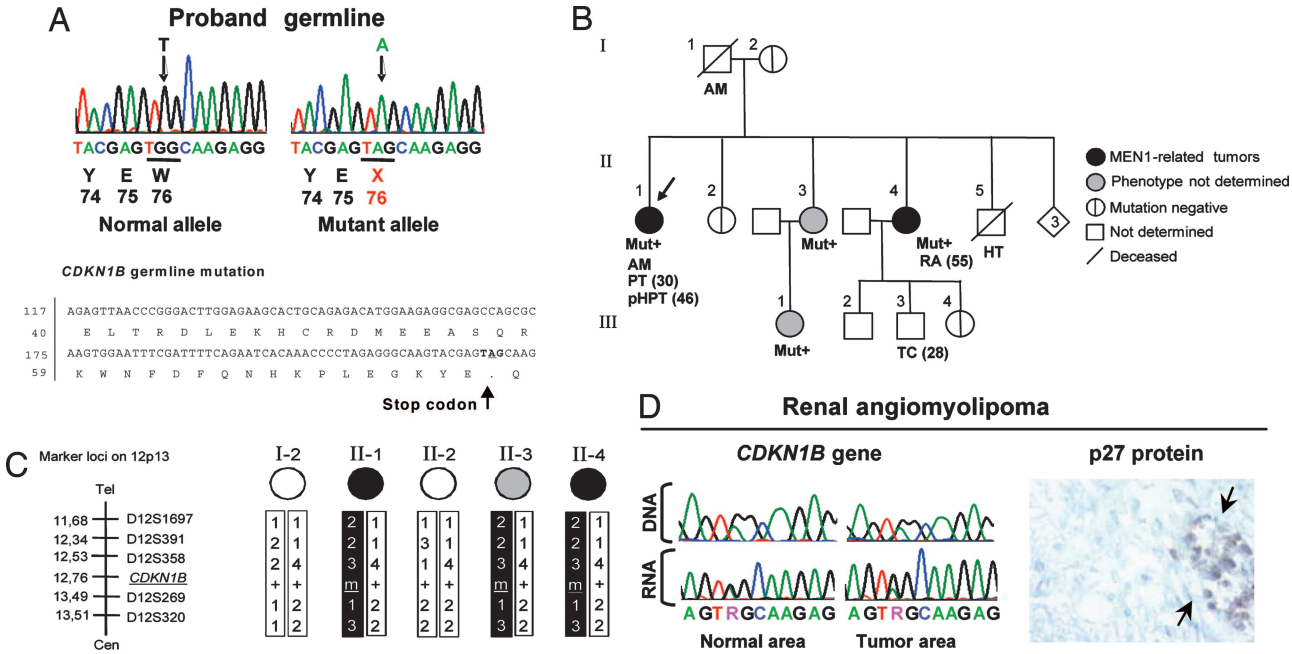

Fig. 3. Identification of a germ-line mutation in *CDKN1B* in a suspected MEN1 patient and segregation analyses. (*A*) A PCR fragment corresponding to part of the *CDKN1B* exon 1 was obtained from the proband and cloned, and both alleles were sequenced separately. (*Upper*) The germ-line of the proband showed a heterozygous nonsense mutation at codon 76 (c. 692G→A). (*Lower*) Shown is the position of the mutation in the *CDKN1B* gene and p27 protein. (*B*) Proband family pedigree. Generation numbers are represented by Roman numerals; individuals are represented by Arabic numerals. The proband is II-1, indicated by the arrow. Mut+, mutation-positive individual; AM, acromegaly; PT, pituitary adenoma; pHPT, primary hyperparathyroidism; RA, renal angiomyolipoma; HT, hypertension; TC, testicular cancer. Age of onset is given in parentheses. (*C*) Haplotype analysis. The microsatellite markers on chromosome 12, and their positions, are indicated on the right. The affected haplotype is indicated in black. (*D*) Analysis of the tumor tissue of individual II-4. (*Left*) Sequencing chromatograms showing the 692G→A mutation in both normal and tumor tissue DNA and RNA. (*Right*) Immunohistochemical staining with an anti-p27 antibody shows lack of p27 protein in the tumor tissue. The arrows indicate infiltrating lymphocytes used as positive control for p27 staining. (Immunoperoxidase original magnification: ×640.)

www.pnas.org/cgi/doi/10.1073/pnas.0609565103

RETRACTION

CHEMISTRY. For the articles "Flexible bilayers with spontaneous curvature lead to lamellar gels and spontaneous vesicles," by Bret A. Coldren, Heidi Warriner, Ryan van Zanten, Joseph A. Zasadzinski, and Eric B. Sirota, which appeared in issue 8, February 21, 2006, of *Proc Natl Acad Sci USA* (103:2524–2529; first published February 8, 2006; 10.1073/pnas.0507024103), and "Lamellar gels and spontaneous vesicles in catanionic surfactant mixtures," by Bret A. Coldren, Heidi Warriner, Ryan van Zanten, Joseph A. Zasadzinski, and Eric B. Sirota, which appeared in issue 6, March 14, 2006, of *Langmuir* (22:2465–2473), the editors of both journals retract these papers because they constitute duplicate publication.

Solomon H. Snyder, Senior Editor, PNAS

David G. Whitten, Editor-in-Chief, *Langmuir*

www.pnas.org/cgi/doi/10.1073/pnas.0609486103